NRC·CNRC

NRC Publications Archive
Archives des publications du CNRC

Circular optical phased array with large steering range and high resolution

Benedikovič, Daniel; Liu, Qiankun; Sánchez-Postigo, Alejandro; Atieh, Ahmad; Smy, Tom; Cheben, Pavel; Ye, Winnie N.

This publication could be one of several versions: author's original, accepted manuscript or the publisher's version. / La version de cette publication peut être l'une des suivantes : la version prépublication de l'auteur, la version acceptée du manuscrit ou la version de l'éditeur.
For the publisher's version, please access the DOI link below./ Pour consulter la version de l'éditeur, utilisez le lien DOI ci-dessous.

Publisher's version / Version de l'éditeur:
https://doi.org/10.3390/s22166135
Sensors, 22, 16, 2022-08-16

NRC Publications Archive Record / Notice des Archives des publications du CNRC :
https://nrc-publications.canada.ca/eng/view/object/?id=f6c692a1-61ca-4638-bf88-36c94ff76479
https://publications-cnrc.canada.ca/fra/voir/objet/?id=f6c692a1-61ca-4638-bf88-36c94ff76479

Access and use of this website and the material on it are subject to the Terms and Conditions set forth at
https://nrc-publications.canada.ca/eng/copyright
READ THESE TERMS AND CONDITIONS CAREFULLY BEFORE USING THIS WEBSITE.

L'accès à ce site Web et l'utilisation de son contenu sont assujettis aux conditions présentées dans le site
https://publications-cnrc.canada.ca/fra/droits
LISEZ CES CONDITIONS ATTENTIVEMENT AVANT D'UTILISER CE SITE WEB.

Questions? Contact the NRC Publications Archive team at PublicationsArchive-ArchivesPublications@nrc-cnrc.gc.ca. If you wish to email the authors directly, please see the first page of the publication for their contact information.

Vous avez des questions? Nous pouvons vous aider. Pour communiquer directement avec un auteur, consultez la première page de la revue dans laquelle son article a été publié afin de trouver ses coordonnées. Si vous n'arrivez pas à les repérer, communiquez avec nous à PublicationsArchive-ArchivesPublications@nrc-cnrc.gc.ca.

National Research Council Canada | Conseil national de recherches Canada

Canada

sensors

MDPI

Article

Circular Optical Phased Array with Large Steering Range and High Resolution

Daniel Benedikovič [1,2,3,*], Qiankun Liu [1], Alejandro Sánchez-Postigo [1,4], Ahmad Atieh [5], Tom Smy [1], Pavel Cheben [6] and Winnie N. Ye [1,*]

1 Department Electronics, Carleton University, Ottawa, ON K1S 5B6, Canada
2 Department Multimedia and Information-Communication Technology, University of Zilina, 01026 Zilina, Slovakia
3 University Science Park, University of Zilina, 01026 Zilina, Slovakia
4 Telecommunication Research Institute (TELMA), Universidad de Málaga, E.T.S. Ingeniería de Telecomunicación, Bulevar Louis Pasteur 35, 29010 Málaga, Spain
5 Optiwave Systems, Inc., Ottawa, ON K2E 8A7, Canada
6 National Research Council Canada, Ottawa, ON K1A 0R6, Canada
* Correspondence: daniel.benedikovic@uniza.sk (D.B.); winnie.ye@carleton.ca (W.N.Y.)

Abstract: Light detection and ranging systems based on optical phased arrays and integrated silicon photonics have sparked a surge of applications over the recent years. This includes applications in sensing, free-space communications, or autonomous vehicles, to name a few. Herein, we report a design of two-dimensional optical phased arrays, which are arranged in a grid of concentric rings. We numerically investigate two designs composed of 110 and 820 elements, respectively. Both single-wavelength (1550 nm) and broadband multi-wavelength (1535 nm to 1565 nm) operations are studied. The proposed phased arrays enable free-space beam steering, offering improved performance with narrow beam divergences of only 0.5° and 0.22° for the 110-element and 820-element arrays, respectively, with a main-to-sidelobe suppression ratio higher than 10 dB. The circular array topology also allows large element spacing far beyond the sub-wavelength-scaled limits that are present in one-dimensional linear or two-dimensional rectangular arrays. Under a single-wavelength operation, a solid-angle steering between 0.21π sr and 0.51π sr is obtained for 110- and 820-element arrays, respectively, while the beam steering spans the range of 0.24π sr and 0.57π sr for a multi-wavelength operation. This work opens new opportunities for future optical phased arrays in on-chip photonic applications, in which fast, high-resolution, and broadband beam steering is necessary.

Keywords: silicon photonics; optical phased arrays; optical antenna; beam forming; beam steering; field-of-view; circular phased arrays; light detection and ranging

check for updates

Citation: Benedikovič, D.; Liu, Q.; Sánchez-Postigo, A.; Atieh, A.; Smy, T.; Cheben, P.; Ye, W.N. Circular Optical Phased Array with Large Steering Range and High Resolution. *Sensors* **2022**, *22*, 6135. https://doi.org/10.3390/s22166135

Academic Editors: Vittorio M.N. Passaro and Francesco De Leonardis

Received: 8 July 2022
Accepted: 12 August 2022
Published: 16 August 2022

Publisher's Note: MDPI stays neutral with regard to jurisdictional claims in published maps and institutional affiliations.

Copyright: © 2022 by the authors. Licensee MDPI, Basel, Switzerland. This article is an open access article distributed under the terms and conditions of the Creative Commons Attribution (CC BY) license (https://creativecommons.org/licenses/by/4.0/).

1. Introduction

Light detection and ranging (LIDAR) has become a core technology for many applications, including environmental monitoring and sensing [1,2], imaging [3], free-space communications [4], and autonomous vehicles [5]. Despite their diverse deployment, traditional LIDAR systems rely on a large amount of discrete optical elements and equipment and, in addition, depend on mechanical mechanisms to fulfil desired functions of beam steering and shaping [6]. These factors promote high production cost, large size, excessive power consumption, and increased complexity while providing only limited steering range, low resolution, and slow scanning rates. From a long-term perspective, with ever-increasing needs for reliability and scalability, bulky and mechanically rotating approaches are difficult to integrate and scale and will inevitably fail to meet the requirements of driving applications.

In contrast, foundry-based integrated silicon photonics offer great potential for chip-scale LIDARs [7–9]. Integrated photonics leverages the maturity of semiconductor micro-

electronics and the recent advances in high performance photonic devices to achieve true monolithic photonic–electronic integration on a single chip.

In the last decade, LIDAR systems based on integrated optical phased arrays (OPAs) have taken a massive leap forward [10–30]. On-chip OPAs can empower solid-state beam steering, allowing for high-resolution and fast scanning. For the most part, OPAs implemented on silicon photonic platforms, silicon-on-insulator (SOI) in particular, have been designed as one-dimensional (1-D) linear [10–16] or two-dimensional (2-D) rectangular [4,17–26] arrays. In these array configurations, beam steering can be achieved through wavelength-tuned millimeter-long antennas [4,25] or by using optical antennas with cascaded- or independently-controlled phase shifter arrangements [21,22]. Although useful techniques for beam steering have been demonstrated using 1-D linear and 2-D rectangular topologies, a range of performance and design issues remain. For example, the standard OPA far-field radiation pattern exhibits large sidelobes as a consequence of the uniform array distribution. The large sidelobes appear when the spacing between two adjacent optical elements is larger than a half of the operating wavelength. This is, however, a common concern in many photonic technologies, regardless of which of the afore-mentioned OPA arrangements is employed. As a result, 1-D linear and 2-D rectangular arrays typically impose limitations on an aliasing-free beam steering and suffer from a restricted field of view (FOV).

To remove the grating sidelobes and improve the beam-steering performance, circular OPAs have been proposed and represent an important choice [31–41]. Surprisingly, only limited preliminary work on photonic implementation of circular array has been reported to date [39–41], apart from bio-inspired solutions [31], non-photonic-based concepts [32], and optimization-driven circular schemes [33–37]. Indeed, compared to the conventional 1-D/2-D counterparts, the use of circular arrays holds great promise to advance the overall steering performance by improving the FOV ideally up to 2π sr.

In this work, we report a comprehensive study on a 2-D OPA using a concentric-ring configuration. More specifically, we numerically investigate two circular array designs, one with 110 elements (*Array #1*) and another with 820 elements (*Array #2*). The proposed circular OPAs are designed to provide beam-steering functions across the *C*-band communication window, ranging from 1535 nm to 1565 nm. Both circular OPAs show excellent beam-steering performance, maintaining a sidelobe suppression level larger than 10 dB, with narrow angular beamwidths of 0.5° (*Array #1*) and 0.22° (*Array #2*). Moreover, circular topology allows the OPA layouts to be implemented with a large element spacing of 9 µm. Unlike in previous developments, our circular arrays utilize surface-emitting antennas with high radiation efficiency and broadband operation, which allows us to operate in a multi-wavelength regime to further increase the OPA steering range. Solid-angle steering of 0.21π sr (*Array #1*) and 0.51π sr (*Array #2*) is obtained for monochromatic operation at a reference wavelength of 1550 nm, while improved steering ranges of 0.24π sr (Array #1) and 0.57π sr (Array#2) are obtained for a multi-wavelength case. This work opens the door for the development of the next-generation OPA systems on a single silicon chip that offer wideband, high-resolution, and fast beam steering.

2. Circular Array Geometry and Array Factor

A schematic diagram of the proposed circular array is shown in Figure 1a. The green spheres represent individual nano-antennas. The antenna layout is shown in Figure 1b. The circular array consists of N concentric rings, and the radius of the respective ring is given by:

$$R_n = R_0 + (n-1)dr \quad (1)$$

where R_0 is the minimum radius of the initial ring, n is the ring number, and dr denotes the radius increment between two adjacent rings. On each ring, there are M antennas with equal angular spacing between two adjacent elements. In total, $M \times N$ elements are radially arranged in the circular array. As we detailed in Ref. [41], the feeding stage of the circular OPA system comprises an efficient input optical interface formed by a circular input

grating coupler [42], followed by short adiabatic waveguide tapers, and output waveguides that connect the phase shifters with individual optical antennas. In particular, the central input coupler consists of a blazed waveguide grating with an *L*-shaped radiation profile and sub-wavelength grating (SWG) metamaterial blocks. The grating coupler design is optimized to match the upward radiation beam to the near-Gaussian profile of the standard single-mode optical fiber (SMF-28). The optical fiber has a mode field diameter of 10.4 µm at $1/e^2$ intensity and nominal wavelength of 1550 nm. The coupling efficiency of the central grating coupler was calculated as a product between the power radiated from the grating and an overlap between the near-field profile of upward radiated beam and a profile of the fiber mode. According to our calculations, the *L*-shaped central grating coupler radiates 86.3% of input power towards an optical fiber situated above the chip, while only 3.8% is diffracted into the bottom silicon substrate. The near-field overlap between the radiated grating beam and the optical fiber mode is estimated to be 76%. As a result, the coupling loss of the central input waveguide coupler is −1.83 dB, calculated for a quasi-transverse electrical polarization and an operating wavelength of 1550 nm.

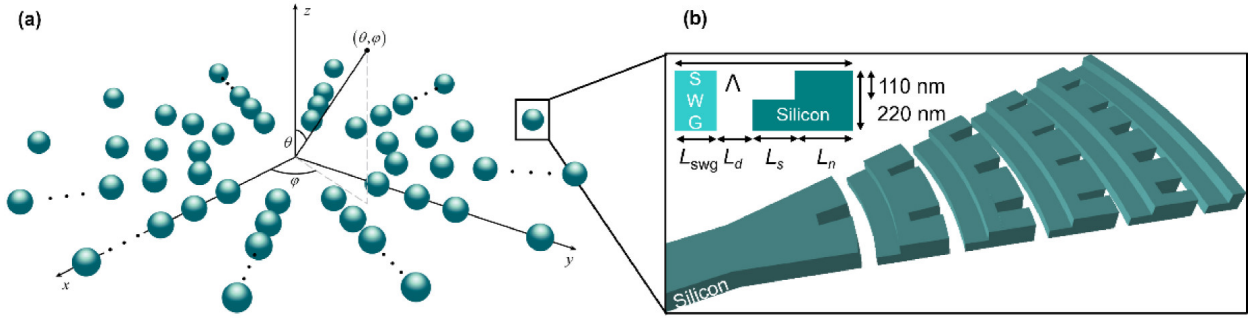

Figure 1. (**a**) Schematic of a two-dimensional circular optical phased array. The green spheres represent individual nano-antennas. (**b**) Three-dimensional schematic of a silicon-based surface-emitting antenna. Inset: Two-dimensional side view of the single antenna period with *L*-shaped radiating segments.

In the following numerical study, we assume isotropic nano-antennas where the signal power is emitted uniformly in all directions. For a circular OPA, the array factor is defined as follows [43,44]:

$$A(\theta,\phi) = \sum_{m=1}^{M}\sum_{n=1}^{N} a_{mn} e^{-i\frac{2\pi}{\lambda}\sin(\theta)\cos(\phi-\frac{2\pi(m-1)}{M})R_n} \quad (2)$$

where the element weight coefficient is $a_{mn} = 1/(M \times N)$, λ is the wavelength, and θ and Φ are the elevation and azimuthal angles, respectively.

To systematically study the performance of the circular array, we calculated the angular beamwidth and sidelobe suppression as a function of four key parameters that determine the array factor: *N*, *M*, R_0, and *dr*. In this work, the angular beamwidth and sidelobe suppression are defined as follows: (i.) the angular beamwidth corresponds to the full width at half maximum (FWHM) of the main lobe and (ii.) the sidelobe suppression expresses the difference between the peak of the main lobe, which is normalized to 0 dB, and the maximum of all other peaks in the scanning range. For numerical simulations, a resolution of 0.01° is considered. The array factor is calculated for a reference wavelength of 1550 nm.

Figure 2 shows the results of a comprehensive study on the effect of the key array parameters (*N*, *M*, R_0, and *dr*) on the circular OPA beamwidth and sidelobes. To determine the array geometry, we varied a selected parameter, while the others remained constant, and assessed the trends in the array performance metrics:

- *Angular beamwidth.* In Figure 2a,c,d, the angular beamwidth of the array factor's main lobe decreases exponentially as the number of rings (N) rises, the minimum ring radius (R_0) increases, and the spacing between two adjacent rings (dr) expands. In contrast, the number of the optical antennas per single ring (M) has a minimum effect (Figure 2b), and thus the angular beamwidth remains virtually constant, or, more likely, its variation is too small to be distinguished with a 0.01° resolution.
- *Sidelobe suppression ratio (SSR).* The sidelobe suppression exponentially increases with the number of concentric rings (N) within an array (see Figure 2a). Moreover, as shown in Figure 2b, the sidelobe suppression increases with the number of elements per ring (M). On top of that, the dependence for even and odd element numbers is apparent. When M is even, as shown by stars in Figure 2b, the circular array is bilaterally symmetric at any direction in the x-y plane, and thus constructive interference of all elements dominates. The sidelobes of each sub-array rise at similar $\{\theta,\Phi\}$ angles, leading to a slightly reduced main-to-sidelobe contrast level. This effect is shown in Figure 3a,b, with the number of elements per single ring being $M = 4$ and $M = 8$, respectively. Here, the level of the sidelobe suppression remains small. The bilateral symmetry is broken when M is odd (shown by dots in Figure 2b). The broken symmetry helps to reduce the magnitude of the grating sidelobes. As a result, the power is distributed more uniformly over the considered angular range with a distinct sidelobe suppression. Last, but not least, the sidelobe suppression is not strongly affected by variations in the minimum ring radius (R_0) (see Figure 2c) as well as in the ring spacing (dr) (see Figure 2d). For example, with R_0 ranging from 0 to 100 µm and dr ranging from 0 to 10 µm, the sidelobe suppression varies from a minimum of about 8 dB up to a maximum of 12 dB. These low variations are likely attributed to the fact that changes in R_0 and dr do not substantially affect the symmetry of the array and have a minimal effect on the element periodicity.

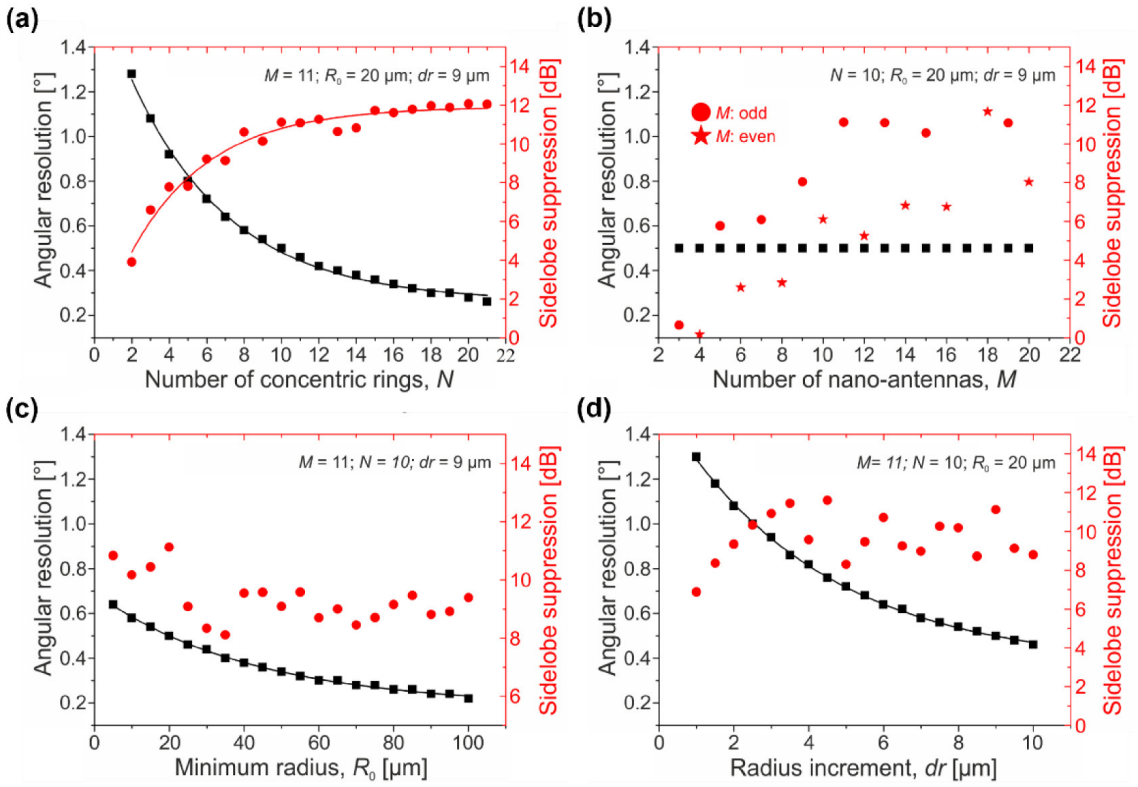

Figure 2. Angular beamwidth and sidelobe suppression of a circular array as a function of (**a**) number of concentric rings, N; (**b**) number of nano-antennas per ring, M; (**c**) minimum radius of rings, R_0; and (**d**) delta radius between two adjacent rings, dr.

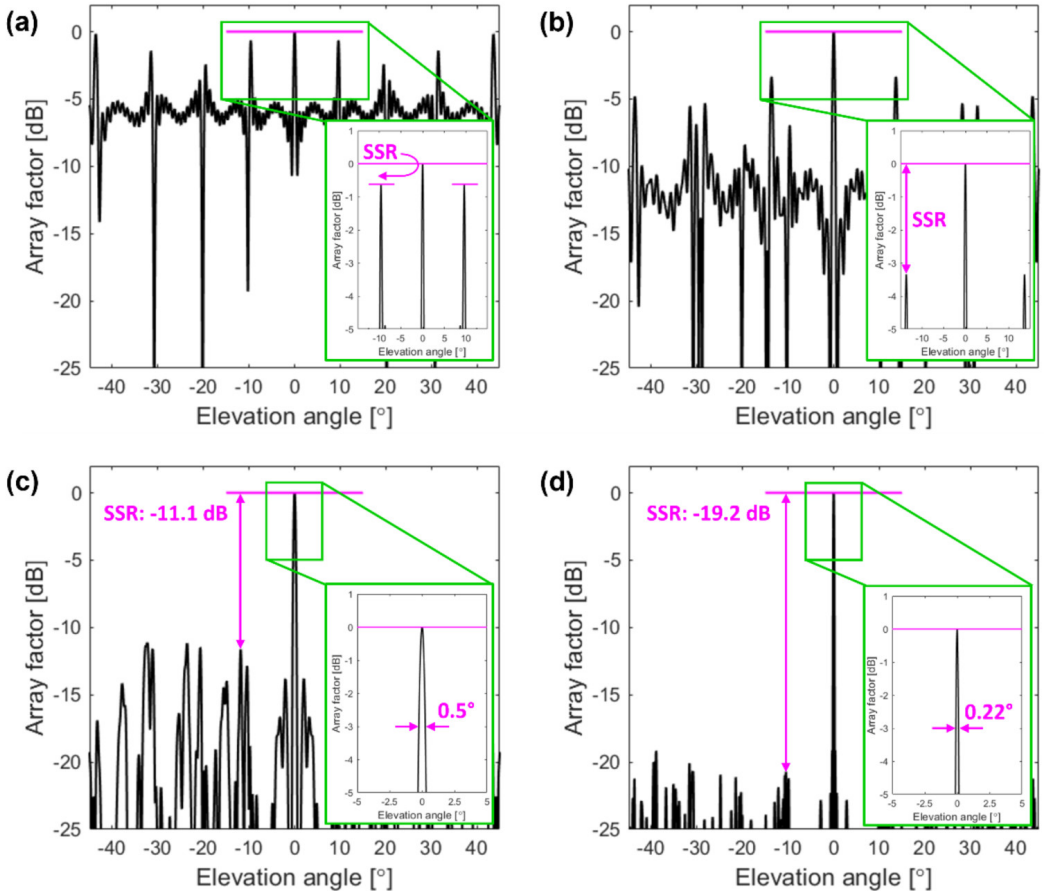

Figure 3. Simulated array factor for different optical phased arrays. Elevation cut ($\Phi = 0°$) of the array factor amplitude for designs with (**a**) $N = 10$, $M = 4$, $R_0 = 20$ µm, and $dr = 9$ µm; (**b**) $N = 10$, $M = 8$, $R_0 = 20$ µm, and $dr = 9$ µm; (**c**) $N = 10$, $M = 11$, $R_0 = 20$ µm, and $dr = 9$ µm (*Array #1*); and (**d**) $N = 20$, $M = 41$, $R_0 = 60$ µm, and $dr = 9$ µm (*Array #2*). Figure insets show the enlarged view of an array factor with an elevation angle θ in a $-5°$ to $5°$ range.

Motivated by the calculations above, we set the following design considerations: a target sidelobe suppression level of -10 dB, a minimum angular beamwidth of 1°, and an inter-element separation (dr) much greater than a half of an operating wavelength to make room for phase shifters [7–10]. According to our analysis, we propose two different circular phased arrays denoted as *Array #1* and *Array #2*, consisting of 110 and 820 elements, respectively. The design parameters of both circular arrays are provided in Table 1.

Table 1. Design parameters of optical phased arrays with circular geometry.

Parameter/ Design	*N*	*M*	R_0 [µm]	*dr* [µm]
Array #1	10	11	20	9
Array #2	20	41	60	9

Figure 3c shows an elevation cut θ of an array factor with $\Phi = 0$ for *Array #1*. We can observe a sidelobe suppression of -11.1 dB, and the estimated angular beamwidth of this circular array is 0.5°. The enlarged view of the main lobe is shown in the inset of Figure 3c. The sidelobe suppression level and the angular beamwidth can be further improved by increasing the total number ($M \times N$) of OPA elements. Figure 3d shows an elevation cut θ of an array factor for *Array #2* with 820 elements. The obtained main-to-sidelobe contrast is substantially improved to -19.2 dB. Furthermore, the increased N of this array also

provides a narrower angular beamwidth of 0.22°, as shown in the inset of Figure 3d. For autonomous vehicle applications, these array features can recognize a 38 cm large object at a distance of about 100 m from the OPA.

Figure 4a shows the array factor for *Array #1* in the *uv* space. The parameters u and v relate to the elevation and azimuthal angles as follows: $u = \sin(\theta)\cos(\Phi)$ and $v = \sin(\theta)\sin(\Phi)$. For the numerical analysis, we considered 1° resolution over the scanning region, corresponding to an entire hemisphere (elevation angle: $\theta = 0°{:}1°{:}90°$, and azimuthal angle: $\Phi = 0°{:}1°{:}360°$).

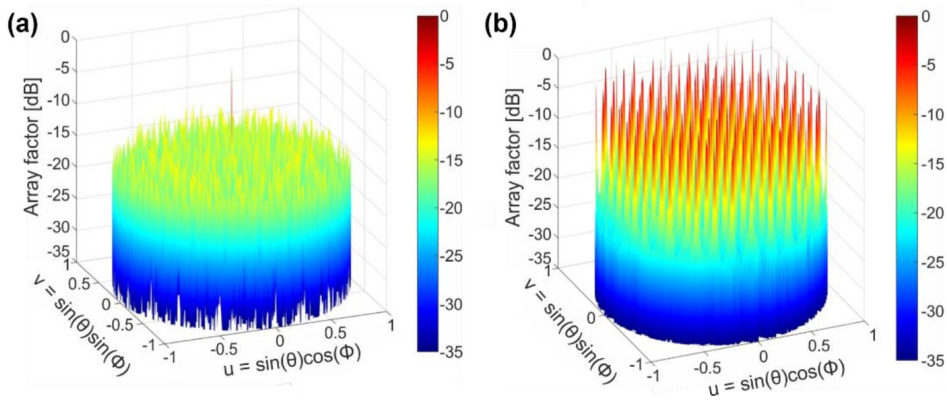

Figure 4. The array factor representation in a *uv* space. (**a**) Circular array: $N = 10$, $M = 11$, $R_0 = 20$ μm, and $dr = 9$ μm at $\theta = 0°$, $\Phi = 0°$. (**b**) Rectangular array: $N = 10$, $M = 11$, $d_x = d_y = 9$ μm at $\theta_A = 0°$, $\Phi_A = 0°$.

To demonstrate the advantages of the circular array topology, in Figure 4 we compare the array factor of a circular array (*Array #1*) with the array factor of a rectangular configuration, both having an identical number of elements and separation distance. For an array with a rectangular layout, the array factor is defined as [43,44]:

$$A(\theta,\phi) = \sum_{m=1}^{M}\sum_{n=1}^{N} a_{mn} e^{-i\frac{2\pi}{\lambda}[d_x \sin(\theta)\cos(\phi) + d_y \sin(\theta)\sin(\phi)]} \quad (3)$$

where M and N denote the number of elements in each row and each column, respectively, and d_x and d_y are element spacings along x and y axis, respectively.

We note that in this rectangular array, the element spacing is set to be the minimum distance between adjacent elements in the circular array, i.e., $d_x = d_y = dr$. As shown in Figure 4a, only the main lobe is visible for a circular array configuration, even though the element spacing is substantially larger than a half of an operating wavelength. On the contrary, large sidelobes are periodically distributed and are consistently dominant over the full scanning region as illustrated in the corresponding rectangular array configuration of Figure 4b. The periodic arrangement of the array and a rectangular element spacing in both directions (which is indeed larger than a half of a wavelength) are responsible for the presence of strong sidelobes and for the low sidelobe suppression ratio.

3. Far-Field Pattern of Circular Array

The array far-field pattern (AFP) of the circular array is defined as follows:

$$\mathrm{AFP} = E(\theta,\phi) \times A(\theta,\phi) \quad (4)$$

where $E(\theta,\Phi)$ is the far field of an individual antenna and $A(\theta,\Phi)$ is the array factor. For practical OPAs, the actual steering range is limited by the grating lobes of the array factor $A(\theta,\Phi)$ and by the far-field pattern of the radiation element, i.e., surface-emitting antenna $E(\theta,\Phi)$. For typical rectangular arrays, the presence of grating lobes is the main restriction as distance between individual elements is much larger than a half of a wavelength. Therefore, the actual steering range of rectangular arrays can be represented by the elevation and

azimuthal angles obtained by the angular location of the grating lobes. For instance, for the rectangular configuration, as shown in Figure 4b, the beam steering is limited to only 9.9° × 90° ($\theta \times \Phi$). In contrast, for arrays with a circular configuration, the grating lobes are effectively suppressed with respect to the main lobe. The beam-steering range is then determined by the far-field pattern of the grating antenna.

To quantify the steering range, we calculate the solid angle Ω_{SR} as:

$$\Omega_{SR} = \iint_{SR} \sin(\theta) d\theta d\phi \quad (5)$$

The Ω_{SR} ranges from 0 to 2π, corresponding to the solid angle of a full hemisphere.

The circular array can be treated as N sub-arrays with M elements, having an element spacing of $R_n \sin(2\pi/M)$. The grating sidelobes of each sub-array arise at different elevation and azimuthal angles $\{\theta, \Phi\}$. The overall array factor is represented by the convolution of an array factor of respective N sub-arrays. Due to this, the constructive interference remains dominant only at the main lobe at the elevation and azimuthal angles $\{\theta_A, \Phi_A\}$. As a result, the circular array can provide a maximum theoretical FOV of 90° × 360° ($\theta \times \Phi$), even with an element spacing that is larger than a half of a wavelength. This steering range leads to a solid angle of 2π sr of a full hemisphere. It is worth noting that the actual FOV remains restricted by the specific radiation pattern of the individual antennas.

4. Antenna Radiation Pattern

In an ideal case, the circular array is formed by isotropic antennas, which ideally yields a maximum theoretical FOV of 2π sr. However, designing such an antenna is not practical. Our proposed optical antenna, schematically shown in Figure 1b, was designed on an SOI platform with 220 nm thick Si waveguide and 2 µm thick buried oxide (BOX) layers. For the upper cladding, we used a silicon dioxide (SiO_2) layer.

The Si antenna has an L-shaped grating profile [45–49] that leverages two asymmetric scatterers, resulting in constructive and destructive interference in the upward and downward direction, respectively. The two-level blazed profile of the optical antenna maximizes radiation efficiency and directionality while at the same time facilitating a broadband device operation. For clarity, the antenna radiation efficiency is defined as the optical power radiated upwards normalized to the input power launched into the waveguide, and the antenna directionality is defined as the ratio between the power radiated upwards and the total out-coupled power (power diffracted upwards and downwards). Using finite difference time domain (FDTD) calculations [50], the diffraction grating was designed to operate with an in-plane input light polarization, i.e., quasi-transverse electric (quasi-TE) polarization. As illustrated in the inset of Figure 1b, along the light propagation direction, the grating period is formed with four radiating segments. The segments are denoted as follows: deep-etch SWG trench (L_{swg}), deep-etch oxide trench (L_d), shallow-etch Si trench (L_s), and unetched Si tooth (L_n). Antenna profile with L-shaped geometry is defined through full- and partial etches with depths of 220 nm and 110 nm, respectively, as both steps are available in standard open-access foundries and multi-project wafer offerings [51,52]. The surface-emitting antenna has five periods, each $\Lambda_a = L_{swg} + L_d + L_s + L_n$ long. The first grating trenches (L_{swg}) are formed by uniform sub-wavelength grating (SWG) nanostructure [53–55] to reduce the return-loss at the waveguide-to-grating interface. The employed SWG geometry synthesizes an equivalent refractive index of 2.32 [41,45,46]. As shown in Figure 1b, the surface-emitting antenna has a curved layout with a total footprint of 2.5 µm × 5.5 µm (width × length).

Figure 5a shows the distribution of the simulated electric field, in particular the real part of E_y field component. Indeed, due to the use of a blazed grating geometry, only a small amount of input power is radiated towards the Si substrate (less than 6% at 1550 nm). Compared to optical antennas implemented on 300 nm thick SOIs [48,56], surface gratings made in a standard 220 nm Si platform have reduced scattering strength per cell unit, and thus the residual transmitted power at the waveguide end remains higher, in this

design case, at about 18%. The antenna far-field pattern, with light emission at 1550 nm, is shown in Figure 5b. The emission angle at 1550 nm is $\{\theta_0 = 6^\circ, \Phi_0 = 0^\circ\}$. Figure 5c shows a simulated out-radiated optical power from the surface-emitting antenna as a function of the wavelength. At 1550 nm, the radiation efficiency and the directionality of an *L*-shaped optical antenna are −1.49 dB (~71%) and −0.36 dB (~92%), respectively. By varying the input wavelength, the optical beam radiated towards an upward direction can be rotated in a 20° range, specifically from −9° ($\theta_0 = 9^\circ$, $\Phi_0 = 180^\circ$) at 1400 nm to 11° ($\theta_0 = 11^\circ$, $\Phi_0 = 0^\circ$) at 1600 nm.

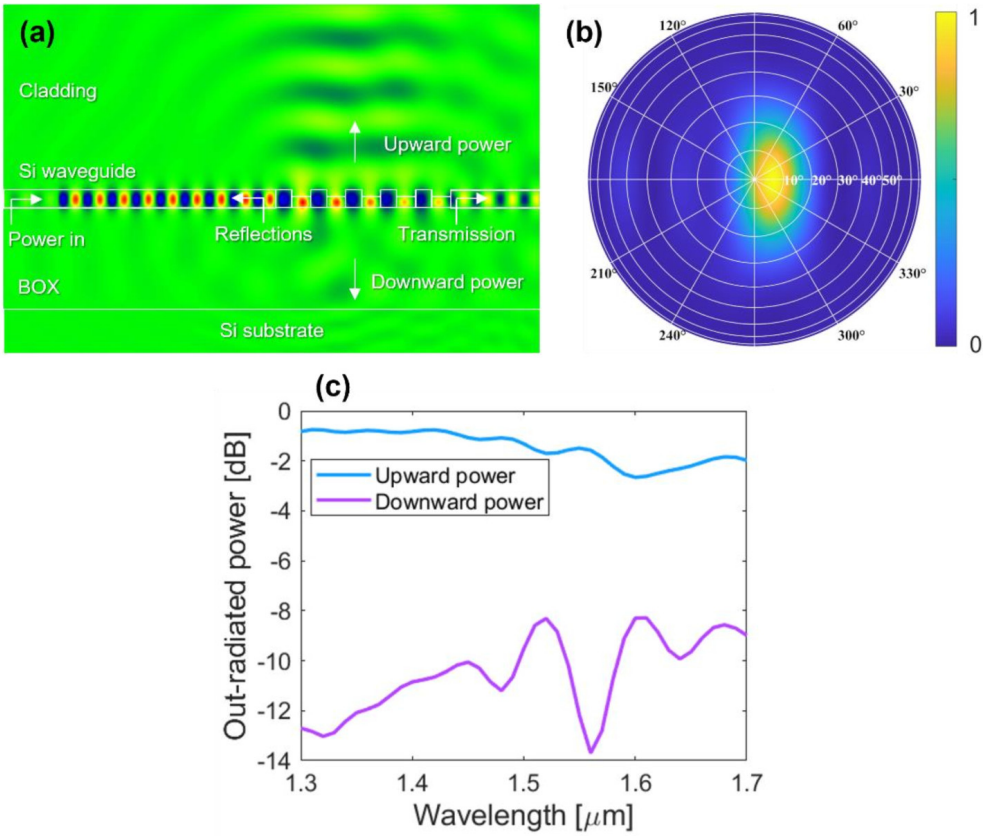

Figure 5. (**a**) Electric field distribution (the real part of E_y field component) of the *L*-shaped optical antenna. (**b**) The antenna far-field pattern, radiating at 1550 nm wavelength. (**c**) Out-radiated power (power up and down) from optical antenna as a function of the wavelength.

5. Beam Formation and Beam-Steering Performance

The circular OPAs are formed such that all the nano-antennas have the same orientation along the *x*-axis. By knowing the OPA layout and antenna far-field pattern we can investigate the beam-steering performance of the OPA. In the following, we first discuss the beam steering of circular OPAs for a monochromatic operation, i.e., the single-wavelength operation, followed by broadband multi-wavelength operation.

In this comprehensive study, we performed numerical simulations of the AFP at different steering angles $\{\theta_A, \Phi_A\}$ over the entire hemisphere. The resolution used in our simulations was set to 1° ($\theta = 0^\circ{:}1^\circ{:}90^\circ$, $\Phi = 0^\circ{:}1^\circ{:}360^\circ$). Figure 6 shows the top view of the calculated AFP in a *uv* space for *Array #1*, operating at a 1550 nm wavelength with steering $\theta_A = 0^\circ$ and $\Phi_A = 0^\circ$, resulting in a radiated beam directed to $\{\theta = \theta_0 = 6^\circ, \Phi = \Phi_0 = 0^\circ\}$.

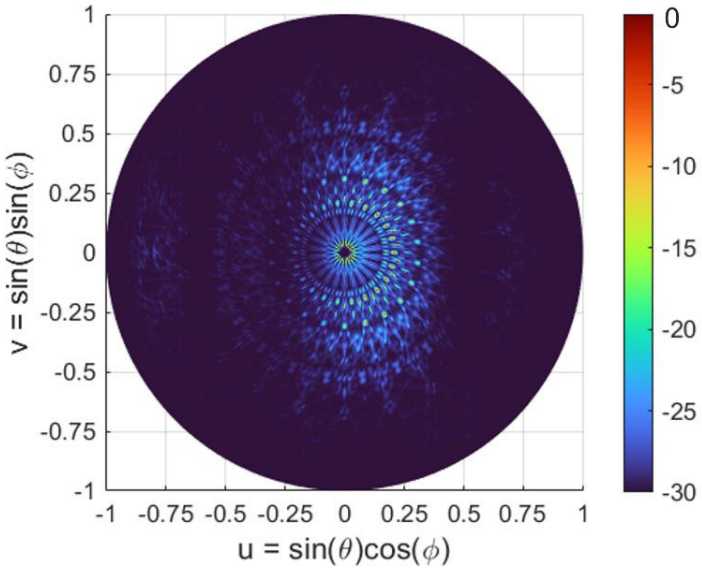

Figure 6. An array far-field pattern representation in a *uv* space for the *Array #1*, with the operating wavelength of 1.55 µm, and steering to $\theta_A = 0°$ and $\Phi_A = 0°$. The peak beam is radiated at $\theta = \theta_0 = 6°$ and $\Phi = \Phi_0 = 0°$.

5.1. Monochromatic Array Operation

In the single-wavelength operation, the antenna radiation pattern, $E(\theta, \Phi)$, remains static, and the steering range of the whole OPA system is limited to the range defined by this pattern. By tailoring the phase of each radiation element via phase shifters, the steering angles $\{\theta_A, \Phi_A\}$ can vary over the entire hemisphere. The steering range is determined as the set of steerable angles $\{\theta, \Phi\}$, for which the level of sidelobe suppression is larger than 10 dB. For the calculated far-field pattern of *Array #1* (shown in Figure 6) and *Array #2*, the sidelobe suppression levels are 12.3 dB and 18.4 dB, respectively. To determine the steering range, all steerable angles are projected on a *uv* plane. Figure 7 shows the projection of the steering range onto a hemisphere for an *Array #1* and an *Array #2*. Both arrays operate at a reference wavelength of 1550 nm. The yellow area represents the set of all steerable angles, with a sidelobe suppression larger than 10 dB. The blue areas, on the other hand, correspond to non-steerable angles. By using Equations (4) and (5), we estimated Ω_{SR} of 0.21π sr for *Array #1* and 0.51π sr for *Array #2*, respectively.

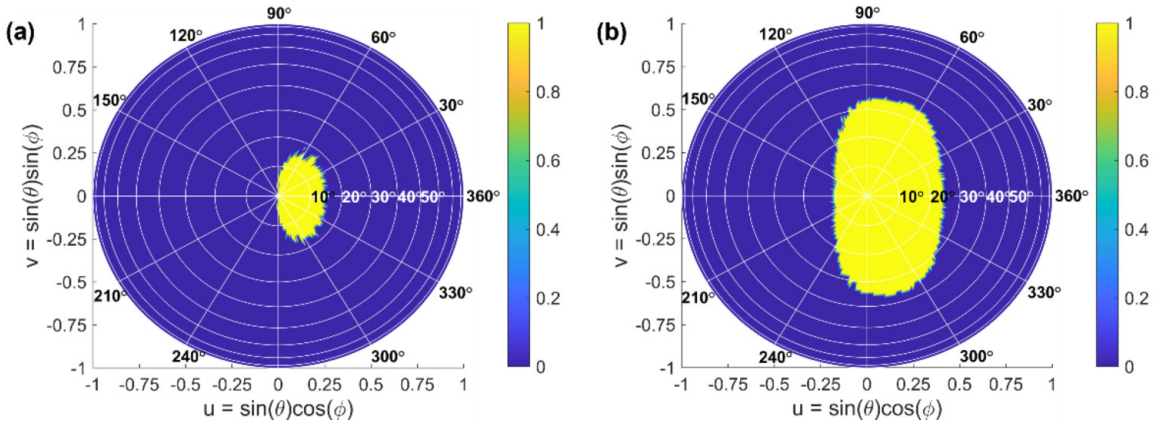

Figure 7. Projection of the steering range onto a hemisphere for (**a**) *Array #1* and (**b**) *Array #2*, both operating at 1550 nm wavelength. The bright area represents the set of all steerable angles, where the sidelobe suppression is larger than 10 dB, and the dark area represents non-steerable angles.

5.2. Multi-Wavelength Array Operation

We now study the steering range in the multi-wavelength operation. As indicated in the previous sections, OPAs with a circular configuration can provide a maximum FOV of 2π sr, and according to Equation (5), the beam-steering range is only limited by the antenna radiation pattern. By wavelength tuning, the antenna radiation pattern can be rotated in the elevation direction. Consequently, the steering range is determined not only by the changes in $\{\theta_A, \Phi_A\}$ via phase adjustments, but also by changes in $\{\theta_0, \Phi_0\}$ via wavelength tuning. A maximum sidelobe contrast can be obtained when the peak angles of the array factor and the antenna far-field pattern coincide, i.e., $\theta_A = \theta_0$ and $\Phi_A = \Phi_0$. Unlike in the monochromatic operation, the beam steering is now optimized in two steps: (i.) by tuning the wavelength such that peak of antenna far-field pattern ($\theta = \theta_0$, $\Phi = 0^\circ$ for $\lambda > 1490$ nm; $\theta = \theta_0$, $\Phi = 180^\circ$ for $\lambda < 1490$ nm) is as close as possible to the target elevation for achieving the largest main-to-sidelobe contrast and (ii.) by modifying the phase of each individual antenna to steer the array factor's main lobe to the target elevation and azimuthal angles.

The study was performed for the *C*-band wavelengths ranging from 1530 nm to 1565 nm. The steerable angles are obtained by determining the level of the sidelobe suppression for the array far-field pattern, which is calculated at different steering angles and wavelengths. Figure 8a,b show the projection of the steering range into a *uv* space for *Array #1* and *Array #2*, yielding solid angles Ω_{SR} of 0.24π sr and 0.57π sr, respectively, over the *C*-band spectral range.

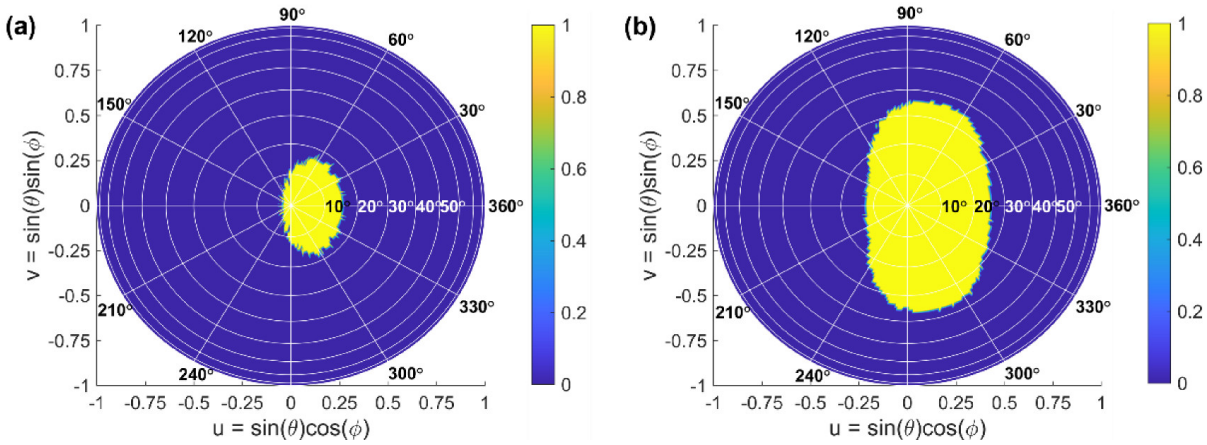

Figure 8. Projection of a steering range for (**a**) *Array #1* and (**b**) *Array #2*, both operating at *C*-band wavelengths. The yellow area represents the set of all steerable angles, where the sidelobe suppression is larger than 10 dB, and the blue area represents non-steerable angles.

6. Power Consumption and Optical Loss in Circular Array

Besides the simplistic OPA layout and geometry and their promising beam-steering function, high-performance phased arrays call upon low-power-consuming elements for phase adjustments and low-loss passive building blocks for light coupling, guiding, and routing on a chip. Thus, for large-scale OPAs realized on a silicon platform, the power consumption and losses are also important design considerations. In the following, we estimate the power consumption of the proposed circular OPAs and we sum up the optical losses for the key passive elements of the proposed circular OPAs.

In waveguide-integrated OPAs, the 2-D beam steering is typically realized by using a phase tuning of waveguides and/or wavelength tuning of an input light source hand-in-hand with individual optical nano-antennas [10–26]. In our OPAs, where the optical nano-antennas are arranged in a grid of concentric rings, thermo-optic phase shifters were considered. They consist of a resistive material situated on top of/near a silicon strip waveguide. Thermal-based phase shifters are easy-to-implement devices, fully compatible with the open-access silicon foundry processing schemes and standard back-end-of-line

(BEOL) metallization steps [51]. The efficiency of a thermal-based phase shifter can be calculated as follows [57–59]:

$$P_\pi = \Delta T_\pi \cdot G \cdot A \tag{6}$$

where G is thermal conductance, A is a waveguide cross-section, and ΔT_π refers to the temperature change to induce a π phase shift. In our case, the strip silicon waveguide is implemented as the phase shifter, having a rectangular cross-section of 220 nm by 500 nm (thickness by width). The temperature shift is defined as [58]:

$$\Delta T_\pi = \frac{\lambda}{2 \cdot L \cdot dn/dT} \tag{7}$$

Here, λ is the operating wavelength (1550 nm, in our design case), L is the length of the silicon strip waveguide for the thermo-optic phase shifter, and dn/dT denotes the thermo-optic coefficient of silicon (dn/dT = 1.804e − 4 K^{-1} at a wavelength of 1550 nm and the nominal ambient temperature of 300 K [60]).

Adopting the analysis and data reported in Refs. [58,59], we estimated the power consumption of a single optical phase shifter as well as the overall power consumption of the proposed OPA design configurations. To this end, we considered different temperature shifts in the waveguide core to induce a π shift by the thermo-optic phase shifter implemented with silicon strip waveguide of different lengths. The temperature shift ΔT was varied in a 5 K to 20 K range. The lengths of the silicon strip waveguide phase shifter were varied between 1 μm and 10 μm, chosen to be consistent with our analysis on the OPA described in Section 2.

Figure 9 shows the estimated power consumption as a function of the waveguide length for different temperature shifts ΔT. From the calculated results, it becomes apparent that the power consumption decreases exponentially with an increasing waveguide length. In particular, Figure 9a shows a power consumption assessed for a single thermo-optic phase shifter. As a nominal showcase, for a 5 μm long phase shifter and temperature change equal to 10 K, the estimated power consumption is 17 mW. Accordingly, as shown in Figure 9b,c, the overall power consumption of the proposed circular OPAs comprising 110 and 820 elements is estimated to be 1.9 W and 14 W, respectively. It is evident that shorter (longer) thermo-optic phase shifters can enlarge (reduce) the overall power consumption of the OPA system. For instance, a 1 μm long phase shifter consumes 430 mW of power. This is indeed a prohibitively large amount of dissipated power in the system for a single phase-controlled phased array element [4,7,15,16]. Correspondingly, the overall consumption of the circular OPAs will reach excessive power levels of 47 W (*Array #1*) and 350 W (*Array #2*), respectively. In contrast, a thermo-optic phase shifter with a length of 10 μm helps to reduce the power consumption down to 4 mW. Consequently, the overall consumption of 110 and 820 circular OPAs can be lowered to power levels of 470 mW and 3.5 W, respectively.

The critical passive elements for light coupling, guiding, and routing of the circular OPA system include [41,61] the central input grating coupler, the optical nano-antennas, the adiabatic waveguide tapers, and the interconnecting waveguides. The summary of the losses for the key passive OPA elements is provided in Table 2.

Table 2. Passive photonic elements in the circular optical phased array.

Component	Central Coupler	Optical Antenna	Adiabatic Taper	Connecting Waveguide *
Loss [dB]	1.8	0.4	0.2	~0

* Note: Sub-dB waveguide loss per cm are assumed in this case, considering state-of-the-art. silicon-foundry-compliant processing [61]. In the proposed circular OPAs, short interconnecting strip waveguides are considered.

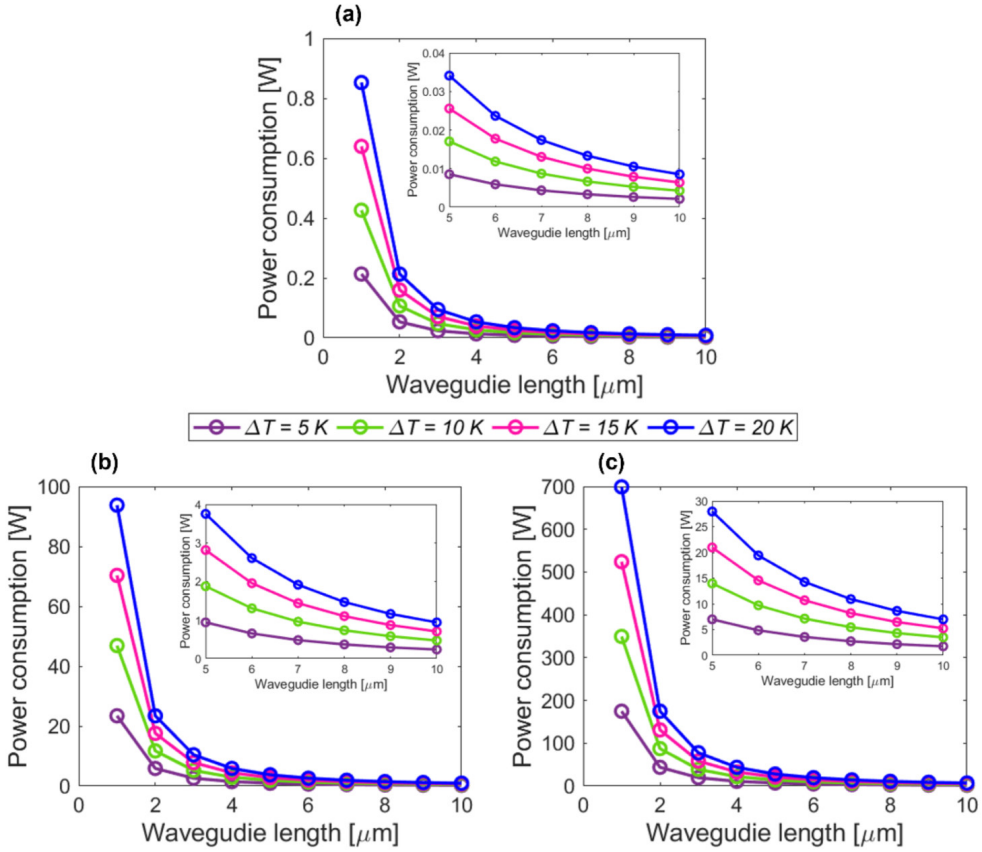

Figure 9. Power consumption analysis versus varied waveguide lengths to implement thermo-optic phase shifters, with a temperature changes ΔT in the 5 K to 20 K range. (**a**) Single thermo-optic phase shifter; circular OPA designs with (**b**) 110 and (**c**) 820 elements, respectively.

7. Conclusions

We proposed and provided a comprehensive study of 2-D OPAs in a circular configuration. Specifically, we numerically investigated two circular array configurations, with 110 elements (*Array #1*) and 820 elements (*Array #2*), for both monochromatic (at 1550 nm) and multi-wavelength operations (in a 1535 nm to 1565 nm range). Circularly arranged OPAs showed substantial improvement over the traditional 1-D linear and 2-D rectangular arrays in beam-steering performance, with a sidelobe suppression contrast larger than 10 dB and with narrow angular beamwidths of 0.5° (for 110-element array) and 0.22° (820-element array). Considering an identical number of antenna elements, circular OPAs enabled an enlarged element spacing of 9 μm compared to their rectangular OPA counterparts. For the nominal 1.55 μm wavelength, the circular OPAs yield solid-angle steering ranges of 0.21π sr (for *Array #1*) and 0.51π sr (for *Array #2*). When the broadband operation was considered, this was further enhanced to 0.24π sr and 0.57π sr, respectively. These results are promising for the next-generation OPA systems realized on a silicon photonic platform with attractive performances in wideband, high-resolution, and fast free-space beam steering.

Author Contributions: Conceptualization: P.C., W.N.Y., Q.L. and A.S.-P.; methodology: Q.L., A.S.-P., D.B., T.S., A.A., P.C. and W.N.Y.; software: Q.L. and D.B.; analysis and discussion: Q.L., A.S.-P., D.B., T.S., A.A., P.C. and W.N.Y.; resources and literature: Q.L., D.B. and W.N.Y.; writing—original draft preparation: Q.L., W.N.Y., T.S., A.A. and D.B.; writing—review and editing: A.S.-P., D.B., W.N.Y., T.S., A.A. and P.C.; visualization: Q.L. and D.B.; supervision: W.N.Y., T.S. and A.A.; project administration: W.N.Y.; funding acquisition: W.N.Y. All authors have read and agreed to the published version of the manuscript.

Funding: This work was supported by the Natural Sciences and Engineering Research Council of Canada's Collaborative R&D Grant Program by collaborating with Optiwave Systems, Inc., Slovak Grant Agency VEGA 1/0113/22, and Slovak Research and Development Agency under the project APVV-21-0217.

Institutional Review Board Statement: Not applicable.

Informed Consent Statement: Not applicable.

Data Availability Statement: Data are contained within the article.

Conflicts of Interest: The authors declare no conflict of interest.

References

1. Bouazizi, M.; Ye, C.; Ohtsuki, T. 2D LIDAR-Based Approach for Activity Identification and Fall Detection. *IEEE Internet Things J.* **2021**, *9*, 10872–10890. [CrossRef]
2. Lv, B.; Xu, H.; Wu, J.; Tian, Y.; Zhang, Y.; Zheng, Y.; Yuan, C.; Tian, S. LiDAR-Enhanced Connected Infrastructures Sensing and Broadcasting High-Resolution Traffic Information Serving Smart Cities. *IEEE Access* **2019**, *7*, 79895–79907. [CrossRef]
3. Zhang, X.; Kwon, K.; Henriksson, J.; Luo, J.; Wu, M.C. A large-scale microelectromechanical-systems-based silicon photonics LiDAR. *Nature* **2022**, *603*, 253–258. [CrossRef] [PubMed]
4. Poulton, C.V.; Byrd, M.J.; Russo, P.; Timurdogan, E.; Khandaker, M.; Vermeulen, D.; Watts, M.R. Long-Range LiDAR and Free-Space Data Communication with High-Performance Optical Phased Arrays. *IEEE J. Sel. Top. Quantum Electron.* **2019**, *25*, 7700108. [CrossRef]
5. Xie, W.; Komljenovic, T.; Huang, J.; Tran, M.; Davenport, M.; Torres, A.; Pintus, P.; Bowers, J. Heterogeneous silicon photonics sensing for autonomous cars [Invited]. *Opt. Express* **2019**, *27*, 3642–3663. [CrossRef] [PubMed]
6. Schwarz, B. Mapping the world in 3D. *Nat. Photonics* **2010**, *4*, 429–430. [CrossRef]
7. Heck, M.J.R. Highly integrated optical phased arrays: Photonic integrated circuits for optical beam shaping and beam steering. *Nanophotonics* **2017**, *6*, 93–107. [CrossRef]
8. Guo, Y.; Guo, Y.; Li, C.; Zhang, H.; Zhou, X.; Zhang, L. Integrated Optical Phased Arrays for Beam Forming and Steering. *Appl. Sci.* **2021**, *11*, 4017. [CrossRef]
9. Sun, X.; Zhang, L.; Zhang, Q.; Zhang, W. Si Photonics for Practical LiDAR Solutions. *Appl. Sci.* **2019**, *9*, 4225. [CrossRef]
10. Hsu, C.P.; Li, B.; Solano-Rivas, B.; Gohil, A.R.; Donzella, V. A review and perspective on optical phased array for automotive LiDAR. *IEEE J. Sel. Top. Quantum Electron.* **2021**, *27*, 8300416. [CrossRef]
11. Doylend, J.K.; Heck, M.J.R.; Bovington, J.T.; Peters, J.D.; Coldren, L.A.; Bowers, J.E. Two-dimensional free-space beam steering with an optical phased array on silicon-on-insulator. *Opt. Express* **2011**, *19*, 21595–21604. [CrossRef]
12. Guo, W.; Binetti, P.R.A.; Althouse, C.; Masanovic, M.L.; Ambrosius, H.P.M.M.; Johansson, L.A.; Coldren, L.A. Two-Dimensional Optical Beam Steering with InP-Based Photonic Integrated Circuits. *IEEE J. Sel. Top. Quantum Electron.* **2013**, *19*, 6100212. [CrossRef]
13. Hutchison, D.N.; Sun, J.; Doylend, J.K.; Kumar, R.; Heck, J.; Kim, W.; Phare, C.T.; Feshali, A.; Rong, H. High-resolution aliasing-free optical beam steering. *Optica* **2016**, *3*, 887–890. [CrossRef]
14. Poulton, C.V.; Yaacobi, A.; Cole, D.B.; Byrd, M.J.; Raval, M.; Vermeulen, D.; Watts, M.R. Coherent solid-state LIDAR with silicon photonic optical phased arrays. *Opt. Lett.* **2017**, *42*, 4091–4094. [CrossRef]
15. Chung, S.W.; Abediasl, H.; Hashemi, H. A Monolithically Integrated Large-Scale Optical Phased Array in Sili-con-on-Insulator CMOS. *IEEE J. Solid-State Circuits* **2018**, *53*, 275–296. [CrossRef]
16. Miller, S.A.; Chang, Y.-C.; Phare, C.T.; Shin, M.C.; Zadka, M.; Roberts, S.P.; Stern, B.; Ji, X.; Mohanty, A.; Gordillo, O.A.J.; et al. Large-scale optical phased array using a low-power multi-pass silicon photonic platform. *Optica* **2020**, *7*, 3–6. [CrossRef]
17. Dostart, N.; Zhang, N.B.; Khilo, A.; Brand, M.; Al Qubaisi, K.; Onural, D.; Feldkhun, D.; Wagner, K.H.; Popović, M.A. Serpentine optical phased arrays for scalable integrated photonic lidar beam steering. *Optica* **2020**, *7*, 726–733. [CrossRef]
18. Li, C.; Cao, X.; Wu, K.; Qiu, G.; Cai, M.; Zhang, G.; Li, X.; Chen, J. Blind zone-suppressed hybrid beam steering for solid-state Lidar. *Photonics Res.* **2021**, *9*, 1871–1880. [CrossRef]
19. Van Acoleyen, K.; Rogier, H.; Baets, R. Two-dimensional optical phased array antenna on silicon-on-insulator. *Opt. Express* **2010**, *18*, 13655–13660. [CrossRef]
20. Sun, J.; Timurdogan, E.; Yaacobi, A.; Hosseini, E.S.; Watts, M.R. Large-scale nanophotonic phased array. *Nature* **2013**, *493*, 195–199. [CrossRef]
21. Abediasl, H.; Hashemi, H. Monolithic optical phased-array transceiver in a standard SOI CMOS process. *Opt. Express* **2015**, *23*, 6509–6519. [CrossRef] [PubMed]
22. Fatemi, R.; Khachaturian, A.; Hajimiri, A. A Nonuniform Sparse 2-D Large-FOV Optical Phased Array with a Low-Power PWM Drive. *IEEE J. Solid-State Circuits* **2019**, *54*, 1200–1215. [CrossRef]
23. Ashtiani, F.; Aflatouni, F. N × N optical phased array with 2N phase shifters. *Opt. Express* **2019**, *27*, 27183–27190. [CrossRef]
24. Zhang, H.; Zhang, Z.; Lv, J.; Peng, C.; Hu, W. Fast beam steering enabled by a chip-scale optical phased array with 8 × 8 elements. *Opt. Commun.* **2020**, *461*, 125267. [CrossRef]

25. Ginel-Moreno, P.; Sánchez-Postigo, A.; De-Oliva-Rubio, J.; Hadij-ElHouati, A.; Ye, W.N.; Wangüemert-Pérez, J.G.; Molina-Fernández, I.; Schmid, J.H.; Cheben, P.; Ortega-Moñux, A. Millimeter-long metamaterial surface-emitting antenna in the silicon photonics platform. *Opt. Lett.* **2021**, *46*, 3733–3736. [CrossRef]
26. Guerber, S.; Fowler, D.; Charlet, I.; Grosse, P.; Abdoul-Carime, K.; Faugier-Tovar, J.; Szelag, B. Development, calibration and characterization of silicon photonics based optical phased arrays. In Proceedings of the SPIE OPTO Smart Photonic and Optoelectronic Integrated Circuits, Online, 6–11 March 2021.
27. Song, Q.; Campione, S.; Boyraz, O.; Capolino, F. Silicon-based optical leaky wave antenna with narrow beam radiation. *Opt. Express* **2011**, *19*, 8735–8749. [CrossRef]
28. Zhao, Q.; Guclu, C.; Huang, Y.; Capolino, F.; Boyraz, O. Experimental Demonstration of Directive Si_3N_4 Optical Leaky Wave Antennas with Semiconductor Perturbations. *J. Light. Technol.* **2016**, *34*, 4864–4871. [CrossRef]
29. Hashiguchi, H.; Kondo, K.; Baba, T.; Arai, H. An Optical Leaky Wave Antenna by a Waffled Structure. *J. Light. Technol.* **2017**, *35*, 2273–2279. [CrossRef]
30. Patel, S.K.; Sorathiya, V.; Guo, T.; Argyropoulos, C. Graphene-based directive optical leaky wave antenna. *Microw. Opt. Technol. Lett.* **2019**, *61*, 153–157. [CrossRef]
31. Pita, J.L.; Aldaya, I.; Santana, O.J.S.; De Araujo, L.E.E.; Dainese, P.; Gabrielli, L.H. Side-lobe level reduction in bio-inspired optical phased-array antennas. *Opt. Express* **2017**, *254*, 30105–30114. [CrossRef]
32. Dal Negro, L.; Boriskina, S.V. Deterministic aperiodic nanostructures for photonics and plasmonics applications. *Laser Photonics Rev.* **2012**, *6*, 178–218. [CrossRef]
33. Zhang, F.; Zhang, D.; Pan, S. Fast and wide-range optical beam steering with ultralow side lobes by applying an optimized multi-circular optical phased array. *Appl. Opt.* **2018**, *57*, 4977–4984. [CrossRef] [PubMed]
34. Manohar, V.; Rahmat-Samii, Y. Revisiting the Appearance of Grating Lobes for Antennas with Circular Periodicity. *IEEE Trans. Antennas Propag.* **2019**, *67*, 5723–5728. [CrossRef]
35. Biulkowski, M.E.; Kurmukur, N.C. A Two-Ring Circular Phased-Array Antenna for Mobile Satellite Communications. *IEEE Antennas Propag. Mag.* **1999**, *41*, 14–23. [CrossRef]
36. Bialkowski, M.E. *Antenna Theory: Analysis and Design*, 4th ed.; John Wiley & Sons, Inc.: Hoboken, NJ, USA, 2016.
37. Noordin, N.H.; Zuniga, V.; El-Rayis, A.O.; Haridas, N.; Erdogan, A.T.; Arslan, T. Uniform Circular Arrays for Phased Array Antenna. In Proceedings of the Loughborough Antennas & Propagation Conference, Loughborough, UK, 14–15 November 2011.
38. Cardoso, R.S.; Oliveira, L.P.; Hernandez-Figueroa, H.E. Assessment of Fermat's Spiral Arrays for Photonic Dielectric Antennas. In Proceedings of the15th European Conference on Antennas and Propagation, Dusseldorf, Germany, 22–26 March 2021.
39. Zeng, S.; Zhang, Y.; Zhu, J.; Wu, Z.; Chen, Y.; Yu, S. 360° on chip optical beam steering based on superposition of planar spiral orbital angular momentum waves. In Proceedings of the Conference on Lasers and Electro-Optics Europe and European Quantum Electronics Conference, Munich, Germany, 23–27 June 2019.
40. Liu, X.; Xiong, B.; Sun, C.; Hao, Z.; Wang, L.; Wang, J.; Han, Y.; Li, H.; Luo, Y. Circular optical phased array for 360° constant amplitude scanning. In Proceedings of the 10th International Conference on Information Optics and Photonics, Beijing, China, 8–11 July 2018.
41. Liu, Q.; Benedikovic, D.; Smy, T.; Atieh, A.; Cheben, P.; Ye, W.N. Circular Optical Phased Arrays with Radial Nano-Antennas. *Nanomaterials* **2022**, *12*, 1938. [CrossRef] [PubMed]
42. Doerr, C.R.; Buhl, L.L. Circular grating coupler for creating focused azimuthally and radially polarized beams. *Opt. Lett.* **2011**, *36*, 1209–1211. [CrossRef]
43. Josefsson, L.; Persson, P. *Conformal Array Antenna Theory and Design*, 1st ed.; John Wiley & Sons, Inc.: Hoboken, NJ, USA, 2006.
44. Orfanidis, S.J. *Electromagnetic Waves and Antennas*, 3rd ed.; Rutgers University: Piscataway, NJ, USA, 2004.
45. Benedikovic, D.; Alonso-Ramos, C.; Pérez-Galacho, D.; Guerber, S.; Vakarin, V.; Marcaud, G.; Le Roux, X.; Cassan, E.; Marris-Morini, D.; Cheben, P.; et al. *L*-shaped fiber-chip grating couplers with high directionality and low reflectivity fabricated with deep-UV lithography. *Opt. Lett.* **2017**, *42*, 3439–3442. [CrossRef]
46. Benedikovic, D.; Alonso-Ramos, C.; Guerber, S.; Le Roux, X.; Cheben, P.; Dupré, C.; Szelag, B.; Fowler, D.; Cassan, E.; Marris-Morini, D.; et al. Sub-decibel silicon grating couplers based on L-shaped waveguides and engineered subwavelength metamaterials. *Opt. Express* **2019**, *27*, 26239–26250. [CrossRef]
47. Kamandar Dezfouli, M.; Grinberg, Y.; Melati, D.; Cheben, P.; Schmid, J.H.; Sánchez-Postigo, A.; Ortega-Moñux, A.; Wangüemert-Pérez, G.; Cheriton, R.; Janz, S.; et al. Perfectly vertical surface grating couplers using subwavelength engineering for increased feature sizes. *Opt. Lett.* **2020**, *45*, 3701–3704. [CrossRef]
48. Khajavi, S.; Melati, D.; Cheben, P.; Schmid, J.H.; Liu, Q.; Xu, D.-X.; Ye, W.N. Compact and highly-efficient broadband surface grating antenna on a silicon platform. *Opt. Express* **2021**, *29*, 7003–7014. [CrossRef]
49. Khajavi, S.; Melati, D.; Cheben, P.; Schmid, J.H.; Xu, D.-X.; Janz, S.; Ye, W.N. Design of compact silicon antennas based on high directionality gratings. In Proceedings of the IEEE Photonics Conference (IPC) 2020, Vancouver, BC, Canada, 28 September–1 October 2020.
50. OptiFDTD from Optiwave Systems, Inc. Available online: https://optiwave.com/ (accessed on 1 May 2022).
51. Rahim, A.; Goyvaerts, J.; Szelag, B.; Fedeli, J.-M.; Absil, P.; Aalto, T.; Harjanne, M.; Littlejohns, C.; Reed, G.; Winzer, G.; et al. Open-access silicon photonics platforms in Europe. *IEEE J. Sel. Top. Quantum Electron.* **2019**, *25*, 1–18. [CrossRef]

52. Benedikovic, D.; Alonso-Ramos, C.; Cheben, P.; Schmid, J.H.; Wang, S.; Xu, D.-X.; Lapointe, J.; Janz, S.; Halir, R.; Ortega-Moñux, A.; et al. High-directionality fiber-chip grating coupler with interleaved trenches and subwavelength index-matching structure. *Opt. Lett.* **2015**, *40*, 4190–4193. [CrossRef] [PubMed]
53. Halir, R.; Ortega-Moñux, A.; Benedikovic, D.; Mashanovich, G.Z.; Wangüemert-Pérez, J.-G.; Molina-Fernández, I.; Cheben, P. Subwavelength-grating metamaterial structures for silicon photonic devices. *Proc. IEEE* **2018**, *106*, 2144–2157. [CrossRef]
54. Cheben, P.; Halir, R.; Schmid, J.H.; Atwater, H.A.; Smith, D.R. Subwavelength integrated photonics. *Nature* **2018**, *560*, 565–572. [CrossRef]
55. Luque-González, J.M.; Sánchez-Postigo, A.; Hadij-ElHouati, A.; Ortega-Moñux, A.; Wangüemert-Pérez, J.G.; Schmid, J.H.; Cheben, P.; Molina-Fernández, Í.; Halir, R. A review of silicon subwavelength gratings: Building break-through devices with anisotropic metamaterials. *Nanophotonics* **2021**, *10*, 2765–2797. [CrossRef]
56. Melati, D.; Kamandar Dezfouli, M.; Grinberg, Y.; Schmid, J.H.; Cheriton, R.; Janz, J.; Cheben, P.; Xu, D.-X. Design of Compact and Efficient Silicon Photonic Micro Antennas with Perfectly Vertical Emission. *IEEE J. Sel. Top. Quantum Electron.* **2021**, *27*, 8200110. [CrossRef]
57. Watts, M.R.; Sun, J.; DeRose, C.; Trotter, D.C.; Young, R.W.; Nielson, G.N. Adiabatic thermo-optic Mach–Zehnder switch. *Opt. Express* **2013**, *38*, 733–735. [CrossRef]
58. Jacques, M.; Samani, A.; El-Fiky, E.; Patel, D.; Xing, Z.; Plant, D.V. Optimization of thermo-optic phase-shifter design and mitigation of thermal crosstalk on the SOI platform. *Opt. Express* **2019**, *27*, 10456–10471. [CrossRef]
59. Bird, R.B.; Stewart, W.E.; Lightfoot, E.N. *Transport Phenomena*, 1st ed.; Wiley: New York, NY, USA, 2006; ISBN 978-0-470-11539-8.
60. Komma, J.; Schwarz, C.; Hofmann, G.; Heinert, D.; Nawrodt, R. Thermo-optic coefficient of silicon at 1550 nm and cryogenic temperatures. *Appl. Phys. Lett.* **2012**, *101*, 041905. [CrossRef]
61. Wilmart, Q.; Brision, S.; Hartmann, J.-M.; Myko, A.; Ribaud, K.; Petit-Etienne, C.; Youssef, L.; Fowler, D.; Charbonnier, B.; Sciancalepore, C.; et al. A Complete Si Photonics Platform Embedding Ultra-Low Loss Waveguides for O- and C-Band. *J. Light. Technol.* **2021**, *39*, 532–538. [CrossRef]